

Simulation studies of the behavior of positrons in a microtrap with long aspect ratio

Alireza Narimannezhad,^{*} Christopher J. Baker, Marc H. Weber, Jia Xu, and Kelvin G. Lynn[†]

Center for Materials Research, Washington State University, Pullman, WA 99164-2711

The charged particles storage capacity of microtraps (micro-Penning-Malmberg traps) with large length to radius aspect ratios and radii of the order of tens of microns was explored. Simulation studies of the motions of charged particles were conducted with particle-in-cell plasma code WARP and the Charged Particle Optics (CPO) program. This paper presents how to reduce simulation noise by optimizing modeling parameters to achieve an equilibrium distribution. The new design of the trap consisted of an array of microtraps with confinement voltages of only 10 V. It was computationally shown that each microtrap with 50 μm radius stored positrons with density higher than a conventional Penning-Malmberg trap ($\approx 10^{11} \text{ cm}^{-3}$). The results of the simulation of a plasma initialized with a uniform density and Boltzmann energy distributions showed that the plasma tends to transform to a soft edge distribution in radial direction as it approaches the equilibrium. The shorter the plasma we had, the faster the equilibrium it reached. The shorter plasma thermalized to a lower final energy. Computationally, more than one hundred million positrons were trapped in one microtrap with 50 μm radius and 10 cm length, and the density scaled as radius⁻² till 3 μm . Ten times higher density was trapped in 50 μm radius microtrap with higher barrier potentials of 50 V.

I. INTRODUCTION

The accumulation and storage of the large quantities of low-energy positrons is becoming increasingly important in different fields. Examples include the study of Bose-Einstein condensation of positronium atoms [1], electron-positron plasma in parameter regimes of relevance in astrophysics [2], low-energy antihydrogen production and its confinement for times larger than 1000 s [3, 4], studies of the fundamental symmetries of nature [5], gravitational interaction of antimatter [6], and materials science [7]. A more ambitious goal might be the use of antimatter traps to store energy at the maximum possible density per mass unit. Antimatter propulsion of spaceships may well be the only viable method to travel beyond the solar system.

Single-component plasmas are the method of choice to accumulate, cool and manipulate a large number of positrons. In principle, these plasmas can be confined by static electric and magnetic fields and be in a state of thermal equilibrium for long periods of time [8]. While a number of devices and protocols have been used and proposed to trap antimatter, the Penning-Malmberg (PM) trap [9, 10], because of its ease of construction and versatility, has been widely applied in storing a large number of charged particles. To accomplish the goal of energy storage, a fundamental limitation of conventional PM traps needs to be overcome: the required electrostatic confining potentials rise to large and unpractical values as the charge stored in a PM trap is increased. A possible solution might be replacing standard traps [aspect ratio $O(10:1)$] with a longer trap to lower the density and avoid the high electrostatic potentials. This is unpractical

^{*} a.narimannezhad@wsu.edu

[†] kgl@wsu.edu

when the trap is $\gg 1$ m. Moreover, increasing the length of the trap can cause some deterioration on the plasma confining time [11]. Therefore, the trap can be chopped into segments and aligned in parallel in a single magnet so the tubes are shielded by Faraday cages around each charge cloud. The retaining potentials are now fixed as more tubes are added for more positrons. In order to make the overall dimensions feasible (avoid $\gg 1$ m diameter of the multi-trap) and still store high densities, each tube diameter was made much smaller, in the order of tens of microns, using MEMS technology as developed for microelectronics. The design of this modified PM trap has been proposed by one of the authors (K. G. Lynn) [12], which consists of an array of microtraps, as shown schematically in Fig. 1, with large length to radius aspect ratio $O(1000:1)$ and low confinement voltage $O(10$ V). Surko and Greaves [13] proposed a multi-cell trap, where each cell has a conventional aspect ratio of 10:1 with a diameter of one centimeter, and its confining voltage is in the order of a few kilovolts.

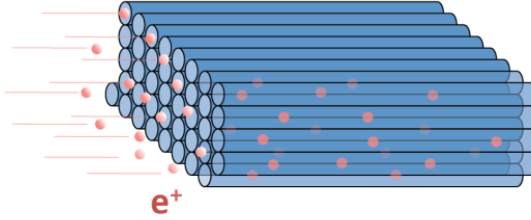


FIG. 1. Schematic configuration of an array of microtraps. The metallic electrodes screen the charge in each microtrap. The image is not to scale.

Generally, there are two restrictions limiting confinement of large number of positrons in PM traps. One is the Brillouin limit, n_B , the maximum density of the plasma confined by a uniform magnetic field \vec{B} , given by [14]

$$n_B = \frac{\epsilon_0 |\vec{B}|^2}{2m}, \quad (1)$$

where m is the rest mass of charge particle and ϵ_0 is the permittivity of free space. For example, the Brillouin density limits us to $n_B \approx 2.4 \times 10^{14} \text{ cm}^{-3}$ in our simulation with the magnetic field of 7 T.

Second limitation is the space charge potential. The total number of particles can be increased by increasing the plasma radius although this radius cannot be simply scaled up because the axial confinement potential becomes large. The space charge potential of the plasma determines the minimum electrical potential required on the end electrodes to confine the plasma in the direction parallel to \vec{B} . In a long, uniform, cylindrical plasma confined with cylindrical metallic electrodes the space charge potential on the axis of the cylinder is calculated as

$$\varphi_0 = \frac{R_p^2 q n}{4 \epsilon_0} + \frac{C^2 R_p^2 q n}{2 \epsilon_0} \ln\left(\frac{R_w}{R_p}\right) = \frac{q N_p}{4 \pi L_p \epsilon_0} \left(2 \ln\left(\frac{R_w}{R_p}\right) + 1\right), \quad (2)$$

where N_p is the number of particles in the plasma and q is the charge of each particle. For example, an extremely large plasma, $N_p = 1.24 \times 10^{13}$, with an initial length, L_p , of 10 cm and a radius, R_p , equal to $R_w/\sqrt{3} = 1$ cm (R_w is the radius of the microtrap) has a positron density of $n = 3.95 \times 10^{11} \text{ cm}^{-3}$. The required minimum end electrode potential is 364 kV based on Eq. (2). The array of microtraps, which is showed earlier, circumvents these large space charge potentials because the metallic electrodes screen the charge in each microtrap. The space charge potential of a microtrap array is compared to a conventional PM trap in Fig. 2. The maximum space charge on axis for each microtrap is 3.75 V. Note that the magnitude of confining electric barrier is linearly increasing with the number of trapped particles in conventional PM trap. The idea to design the trap which consists of an array of microtraps is mainly to avoid the financial cost of an exceedingly high repulsive electric barrier and improve the portability of these traps.

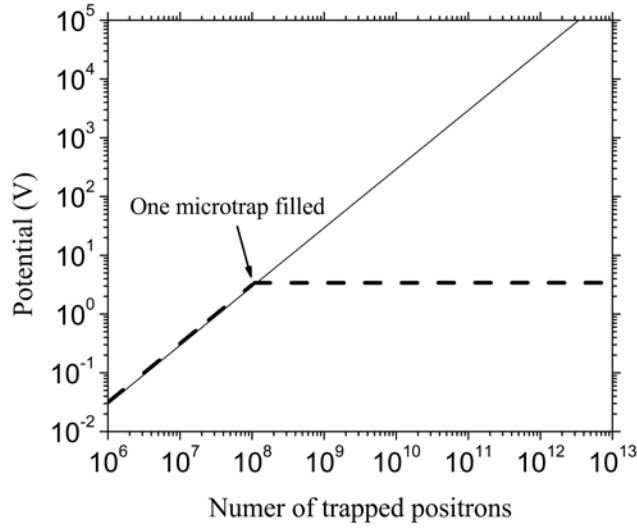


FIG. 2. Space charge potential developed in a microtrap array, the dashed curve, compared to a conventional PM trap, the solid curve, assuming that the array is filled sequentially up to 10^8 positrons per tube, calculated from Eq. (2) when $R_p = R_w/\sqrt{3}$, $R_w = 50\text{ }\mu\text{m}$ and $L_p = 10\text{ cm}$.

A non-neutral plasma in a PM trap with rotational symmetry along the z axis is to reach an equilibrium configuration, in which there is no torque on the plasma and no transport across the magnetic field and it can be confined for an infinite time in principle. In an equilibrium configuration, which can be obtained up to the Brillouin density, the inward Lorentz force is balanced with the outward centrifugal and electric force on the plasma and the plasma rotates rigidly along the z axis [15]. In this work, the positron storage capacity of microtraps with large length to radius aspect ratios and with radii of the order of tens of microns is explored by simulation.

II. SIMULATION MODEL

Analytical extrapolation of Eq. (2) suggests that for a given length of each trap ever smaller trap diameters and larger numbers of parallel traps occupying a fixed volume result in continuously better storage conditions. In the extreme case, replacing a single trap with 1.24×10^{13} positrons with 1.24×10^{13} traps containing one positron each avoids all plasma complications (e.g. pushing near the Brillouin limit, space charge, etc.) and permits storage times limited only by vacuum conditions. Computer simulations of single component plasmas were initiated to explore this ideal trend and see if the simulation can track an initial density distribution to the equilibrium and if it is possible to store positrons in traps with long aspect ratios for long times.

Specifying the equilibrium configuration of non-neutral plasma in the PM traps is not achievable analytically and so it is important to compute the equilibrium state for a specific trap and plasma. In the real world, positrons which are transferred into the microtrap with energies of a few electronvolts will cool via synchrotron radiation, collisions, and image charge effects [16]. In this

paper, we evaluated the maximum number of positrons that can be stored in a trap with large aspect ratio and 3 to 50 micrometer diameters.

A schematic of one microtrap which is modeled in our simulations is shown in Fig. 3. It is composed of a central conducting grounded tube and two end electrodes. The gap between the tube and the end electrodes is comparable to the mesh size defined in the simulation program so that two electrodes with different potentials are as close as possible without touching. The tube is immersed in a uniform magnetic field parallel to the axis of the tube. The typical modeling parameters are listed in Table I.

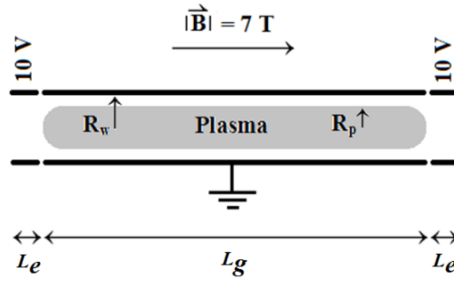


FIG. 3. The schematic geometry of a microtrap and a plasma. The image is not to scale.

TABLE I. The modeling parameters for the simulation of one microtrap. Those without magnitudes are varied.

Modeling parameters	Symbol and/or magnitude
Magnetic field	7 T
Grounded central tube length	L_g
End electrode length	L_e
The radius of the microtrap	$R_w = 3$ to $50 \mu\text{m}$
Conducting tube potential	$V_w = 0 \text{ V}$
End electrode potential	$V_e = 10 \text{ V}$
Initial plasma radius	$R_p = R_w / \sqrt{3}$
Initial plasma length	L_p
Initial space charge potential on the axis	ϕ_0
The initial plasma density	n
Initial plasma three-dimensional temperature	T_0

Modeling simulations were carried out with two different computational tools: WARP code, used extensively in plasma physics [17], and Charged Particle Optics program (CPO) [18]. Simulations conducted within $50 \mu\text{m}$ and $10 \mu\text{m}$ radius microtraps are discussed in detail in Section III and IV, respectively. All the parameters beside those shown in Table I are listed in Tables II and III. Shorter time modelings, cases S1-S8, presented in Fig. 4 were done using given parameters and then the figures of lost particles versus time are fitted with exponential decay function to get the values of lost particles at infinite time. As the microtrap radius decreased, we had to reduce its length to keep the aspect ratio small enough in order to get the results in timely manner because a longer microtrap means higher number of particles and mesh cells. All of the WARP short simulations used parallel processing of eight 2.53 GHz Intel® Xeon® CPUs, while for long runs, cases W1 to W9, modeling used 9 nodes of WSU's high performance computer [19]; totaling 108 Intel(R) Xeon(R) CPUs each running at 2.4 GHz. All the CPO simulations used a 3.2 GHz Intel® Xeon® CPU. We will show in section III how the length of the microtrap affected the simulation time and relaxation time of the plasma towards the equilibrium although there is no change in the trapped density for different lengths. The startup parameters of the plasma played a vital role in reducing the computational effort. The closer the initial guesses of the plasma density distribution and spatial distribution, the faster the codes probed the long term evolution of the plasma in a given trap geometry. However, the major simulation parameters such as time step and mesh size should be chosen carefully and discordant values of them cause a large numerical instability. In the plasma simulation, the Courant-Friedrichs-Lowy (CFL) condition [20] requires that the particles must not move further than one mesh size during one time step.

TABLE II. The parameters used in WARP simulations. Δt , ΔR , PW, and SIM stand for time step, mesh size, positron weight^a, and simulation, respectively.

Modeling parameters												SIM time	Real time	e^+ lost
Case No.	R_w (μm)	Δt (ps)	ΔR (μm)	PW	T_0 (eV)	Φ_0 (V)	n (cm ⁻³)	L_e (cm)	L_g (cm)	L_p (cm)	(μs)	(hr)	(%)	
S1	3	0.5	0.24	5	0.025	2.76	9.76×10^{13}	0.5	0.3	0.27	0.1	14	1.20	
S2	5	1	0.23	4	0.025	3.05	3.99×10^{13}	0.5	0.5	0.45	0.02	13	0.15	
S3	15	5	0.84	20	0.025	2.76	3.99×10^{12}	0.5	3	2.7	0.05	12	0.16	
S4	30	8	1.88	20	0.025	2.76	9.95×10^{11}	0.5	6	5.4	0.08	28	0.20	
S5	50	10	3.35	10	0.025	3.05	3.95×10^{11}	0.5	10	9	0.2	22	0.14	
W1	50	20	6.67	48	0.5	3.75	4.80×10^{11}	0.5	10	9.998	0.2	0.3	64	
W2	50	5	6.67	48	0.5	3.75	4.80×10^{11}	0.5	10	9.998	4	24	0.001	
W3	50	2.5	3.35	48	0.5	3.75	4.80×10^{11}	0.5	10	9.998	12	236	0.003	
W4	50	2.5	3.35	48	0.5	3.75	4.80×10^{11}	0.5	1	0.998	4	11	0.001	
W5	50	2.5	3.35	5	0.5	3.75	4.80×10^{11}	0.5	0.5	0.498	10	94	0.0002	
W6	50	2.5	3.35	5	0.5	37.5	4.80×10^{12}	0.5	0.1	0.098	2.5	47	63.18	
W7	50	2.5	3.35	5	0.5	75	9.60×10^{12}	0.5	0.1	0.098	2.5	47	79.80	
W8	50	2.5	3.35	5	0.5	150	1.92×10^{13}	0.5	0.1	0.098	2.5	47	89.10	
W9 ^b	50	2.5	3.35	5	0.5	37.5	4.80×10^{12}	0.5	0.1	0.098	1.3	35	0.0002	
W10	10	0.5	0.67	9	0.5	3.75	1.20×10^{13}	0.5	0.5	0.498	3	141	3	
W11	10	0.5	0.67	1	0.5	3.75	1.20×10^{13}	0.1	0.5	0.098	1	90	0.011	

^aThe number of real particles that each simulation macro-particle represents.

^bThe end electrodes potential was 50V in this case.

TABLE III. The parameters used in CPO simulations. N_r , SCTD, and E_K are the number of rays, space charge tube diameter, and kinetic energy, respectively.

Modeling parameters														SIM time	Real time	e^+ lost
Case No.	R_w (μm)	Δt (ps)	ΔR (μm)		L_e (mm)	N_r	n (cm ⁻³)	Φ_0 (V)	L_g (cm)	SCTD (μm)	E_K (eV)	(ns)	(hr)	(%)		
S6	1	1	0.05	0.05	5	0.1	64	2.36×10^{12}	0.007	0.2	0.25	5	95	190	46	
S7	3	8	0.1	0.1	10	0.1	64	1.51×10^{12}	0.04	1	0.75	5	300	70	32	
S8	50	10	5	5	50	10	49	2.10×10^{10}	0.16	10	12.5	5	430	24	9	
C1	50	0.4	-	-	-	10	1	4.80×10^{10}	0.375	36	57.7	5	700	20	-	
C2	50	0.4	-	-	-	10	1	1.30×10^{11}	1	36	57.7	5	700	20	-	
C3	50	0.4	-	-	-	10	1	4.80×10^{11}	3.75	36	57.7	5	700	20	-	

^aThe diameter of a cylindrical tube in which the desired charge is uniformly deposited.

Calculating the density of the plasma in a microtrap with specific radius, Eq. (2) takes the form

$$n = \frac{4\pi\epsilon_0\phi_0}{qR_w^2(2\ln(\frac{R_w}{R_p})+1)}, \quad (3)$$

in which the density is inversely proportional to R_w^2 with the fixed ϕ_0 and a constant value of R_w/R_p . The density in a microtrap is then calculated considering its whole volume. For example, if $R_w/R_p = \sqrt{3}$ and ϕ_0 is 3.75 V, the density in one microtrap will be $1.6 \times 10^{11} \text{ cm}^{-3}$ in the one with radius $R_w = 50 \mu\text{m}$. When the radius of the microtrap is decreased, the analytical density in an individual microtrap increases for a constant space charge potential and constant ratio R_w/R_p . If there is an array of individual microtraps to build the trap and the fill factor¹ and the trap volume are constant, the number of trapped particles in the trap is also inversely proportional to R_w^2 with the fixed ϕ_0 and a constant value of R_w/R_p . Results of WARP simulation showed that plasma density follows the expected power law with respect to the microtrap radius (i.e. $n \approx K_{WARP}R_w^{-2}$), as shown in Fig. 4, suggesting that the Brillouin limit may be surpassed at 1 μm radius microtrap while the space charge potential is only 3.75 V. Results from short CPO simulations exhibited an increasing density with a lower rate ($n \approx K_{CPO}R_w^{-1}$). If we rewrite the Eq. (3) as $n = K_{Anal.}R_w^{-2}$, the ratios of $K_{WARP}/K_{Anal.}$ and $K_{CPO}/K_{Anal.}$ will be equal to 1 and 0.07 respectively, showing that the magnitudes of the WARP results are equal to the analytical line while the CPO results pose more than 10 times smaller values. The CPO results should be considered with caution and will be discussed in section V.

¹ The fraction of total volume of microtraps to the trap volume.

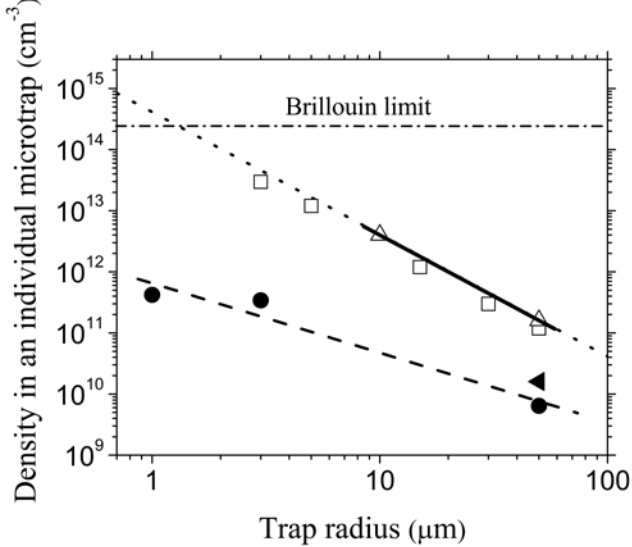


FIG. 4. The density of the plasma as a function of the radius of the microtrap when $R_w/R_p = \sqrt{3}$. The results from short cases S1-S5 of WARP are shown, \square . The cases W5 and W11 of WARP, Δ , and also the cases S6-S8 of CPO, \bullet , are fitted with $\ln(n) = A + B \ln(R_w)$, the solid line and the dashed line respectively, enabling the comparison with the analytical expectation, the dot line.

The WARP data calculates $A = 14.6$ and $B = -2$, and the CPO data calculates $A = 11.812 \pm 0.273$ and $B = -1.136 \pm 0.268$. Well studied case of CPO (the case C2), \blacktriangleleft , for 50 μm radius microtrap is discussed in section V.

III. DESCRIPTION AND RESULTS OF WARP SIMULATION OF THE 50 μm RADIUS MICROTAP

In this section we describe the 50 μm radius microtrap simulation, discussing how to choose the major parameters of the simulation which have the largest influence on numerical noise, how to lower the noise, and how to obtain a computational equilibrium. The configuration and dimensions of this microtrap, as well as the magnitudes of magnetic field and electrostatic potentials are consistent with the experimental setup being studied by our research group [21].

In WARP, the particle-in-cell (PIC) method is employed, which uses the Lorentz equation of motion to advance macro-particles (the particles in the simulation, which represent a discrete specific number of real particles) in time. Following the advancement in time, the new charge density is calculated via a linear interpolation of the macro-particles position onto a mesh and, by solving Poisson's equation, the new electrostatic potential is calculated from the new charge density. The artificial numerical collisions currently included in the WARP simulations are an approximation to realistic collisions and help to introduce another element of realism to the simulations [22].

Since the microtrap in the simulation has rotational symmetry, the two dimensional version of WARP code was used with a R-Z field solver and Neumann boundary conditions (i.e. constant

potential on boundaries) were applied to the conducting walls and end electrodes. The influence of parameters on the simulation progress is discussed in detail in the following sections.

A. ENERGY DISTRIBUTION

The initial energy distribution is chosen as a Boltzmann distribution in WARP program. The initial energy histogram, with bins of 2×10^{-4} eV, for a plasma with 0.5 eV temperature is shown in Fig. 5. Analytical Boltzmann distribution is also shown for comparison. We will show how this distribution evolves and temperature changes during the simulations.

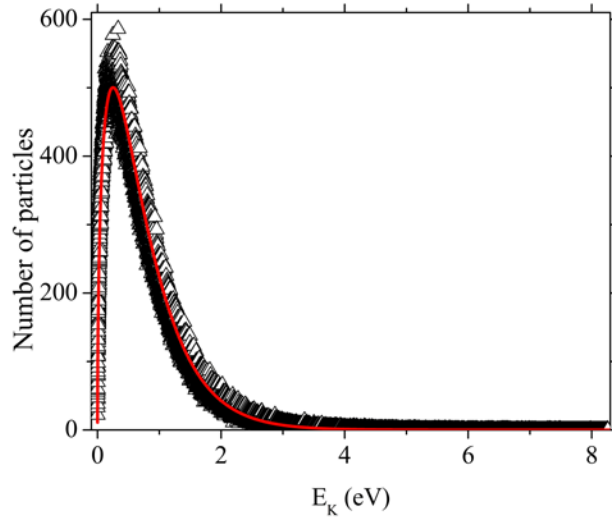


FIG. 5. Boltzmann initial kinetic energy histogram, Δ , with 2×10^{-4} eV bins, of uniform plasma with 0.5 eV temperature. The analytical Boltzmann distribution, —, is shown for comparison at the temperature of 0.5 eV.

B. PLASMA INITIAL LENGTH AND AXIAL DENSITY DISTRIBUTION

In order to obtain the equilibrium state in shorter simulation times, the initial distribution of the plasma should be close to the expected equilibrium distribution. The initial length of the plasma, as well as the plasma density near the two end electrodes, affects the evolution of the plasma toward the equilibrium. Rapid density oscillations occur in the early stages of simulation if the initial length of the plasma is shorter than the length of the grounded central tube ($(L_g - L_p) \gg 1$ mm) or the plasma density has a hard edge profile at the ends. Particles located initially at the ends of the plasma column accelerate outwards and are then reflected by the end electrodes. These fluctuations create potential gradients and result in heating of the plasma. Subsequently, the higher number of fast particles violate the CFL condition and cause numerical instabilities. In our simulation, the plasma was initially 10 μm away from each end of the grounded central tube

while a "cigar" shape distribution, a built-in function of WARP, was used as the starting configuration of the plasma ends. The initial axial potential for this cigar shape plasma in addition to the end cap potential is shown in Fig. 6. The line charge is constant in the center and falls off parabolically at the two ends on a length scale comparable to the radius of the microtrap [17]. There were small density oscillations at $t = 0$, whose magnitude did not increase with time.

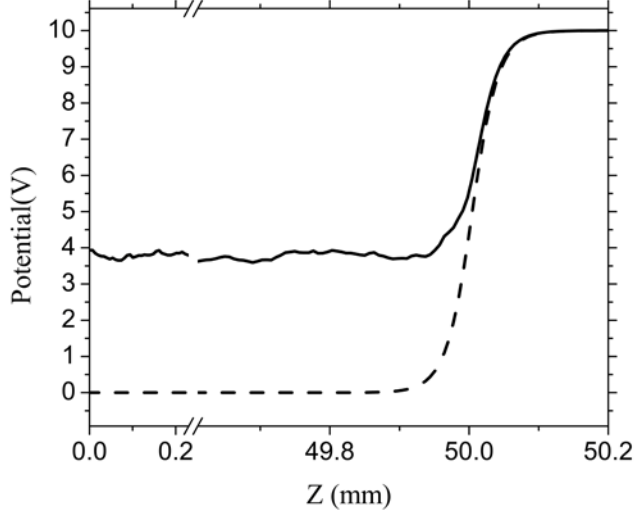


FIG. 6. The initial potential transition on axis from the center of the trap ($z = 0$) to the end electrode which begins from $z = 50.007$ mm, of an empty microtrap, the dashed line, and a microtrap containing a plasma with cigar shape ends, the solid line.

C. POSITRON WEIGHT

The positron weight is the number of real particles that each simulation macro-particle represents. A sufficiently large value of the positron weight is required to reduce the computation time. On the other hand, a smaller number of the positron weight helps the plasma to go toward the computational equilibrium. It has previously shown [22] that if the initial number of macro-particles per cell is of the order of unity or less, typical axial oscillations are relatively small due to the high level of numerical collisions. The positron weight was chosen to be 48 in simulation cases W1-W4 so the initial number of macro-particles per mesh cube cell is about $\frac{1}{3}$. We will show that simulation using this small value of ratio experienced no obvious axial oscillation in the results. However, as we will discuss later in this section, this ratio was chosen ten times higher in the cases W5-W9 in order to eliminate the observed numerical heating.

D. TIME STEP

The particle motion is nearly a guiding center motion when the plasma is immersed in a high magnetic field. Therefore, in general, WARP allows the time step to be larger than the gyro period, τ , and still correctly calculates the various drifts [23] during the simulation. However, the size of the time step was more important in the simulation of plasmas in the microtrap, and not choosing a sufficiently small value caused a high degree of heating effect. In order to confirm that large time step approximation is not valid in our simulation, two different time steps were chosen, 20 ps in the case W1 and 5 ps in the case W2, one was larger than the gyro period and the other equal to the gyro period of the positron in a magnetic field of 7 T. The gyro period was calculated from

$$\tau = \frac{2\pi m}{q |B|} \approx 5 \text{ ps.} \quad (4)$$

In Fig. 7, the number of positrons in a microtrap is plotted as a function of time for the two different time steps. When the time step was 20 ps, about 64% of positrons drifted outwards and annihilated on the cylinder wall within 120 ps in the case W1. No positrons were lost after 120 ps when the time step was reduced to 5 ps in the case W2. The radial density profile is plotted in Fig. 8 after 80 ps to illustrate the behavior of the plasma. The radius of the plasma reached the cylinder for the case W1 with 20 ps step time while it expanded by about 3 μm for the case W2 with 5 ps step time. In other words, when time step was 20 ps, the plasma expanded with an average rate of almost 1000 ms^{-1} , whereas when time step was 5 ps, the average expansion rate was about 40 ms^{-1} . This is a large numerical instability caused by choosing discordant values of times step and mesh size. With a time step of 20 ps, the CFL condition is violated when the velocity of the particle exceeds $\Delta R / \Delta t = 3.35 \times 10^5 \text{ ms}^{-1}$. Figure 9(a) illustrates that more than 25% of particles violated the CFL condition at $t = 0$. This violation caused a numerical instability leading to the fast radial expansion of the plasma at the earliest stages of simulation. As shown in Fig. 9(b), at $t = 0$ and also at $t = 80 \text{ ps}$, only a small portion of the total number of particles ($5 \times 10^{-4} \%$) violated the CFL condition ($\Delta R / \Delta t = 1.34 \times 10^6 \text{ ms}^{-1}$) when the time step was reduced to 5 ps. Therefore, the simulation of traps with at least one small dimension, which requires small mesh sizes, needs small time steps (especially for higher energy particles). This required the use of a large number of CPUs and involved using a different WARP input/output script to run on a high performance computer extended to weeks of running time.

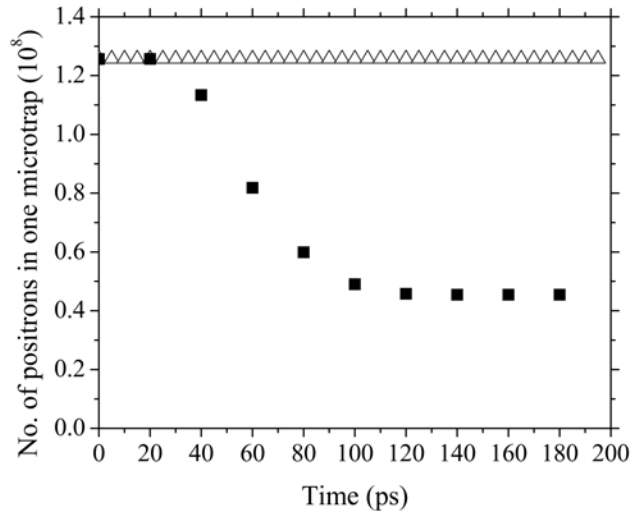


FIG. 7. The number of positrons in one microtrap versus time, for the case W1 with $\Delta t = 20$ ps, \blacksquare , and for the case W2 with $\Delta t = 5$ ps, \triangle .

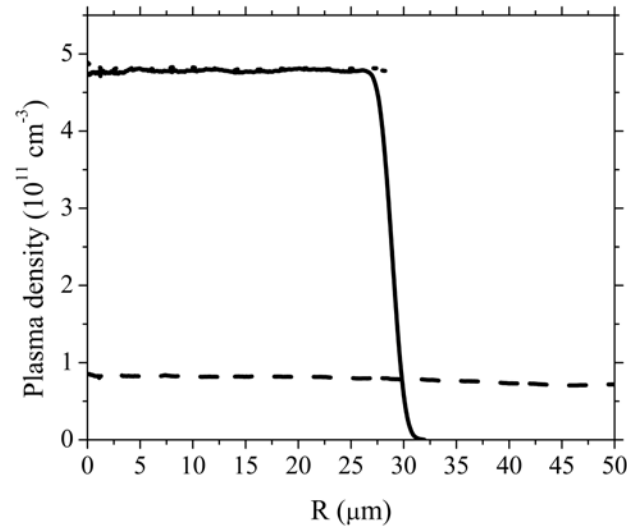


FIG. 8. The radial density profile at $t = 80$ ps for the case W1 with $\Delta t = 20$ ps, dashed line, and for the case W2 with $\Delta t = 5$ ps, solid line. The density profile is also shown at $t = 0$, dot line, for comparison.

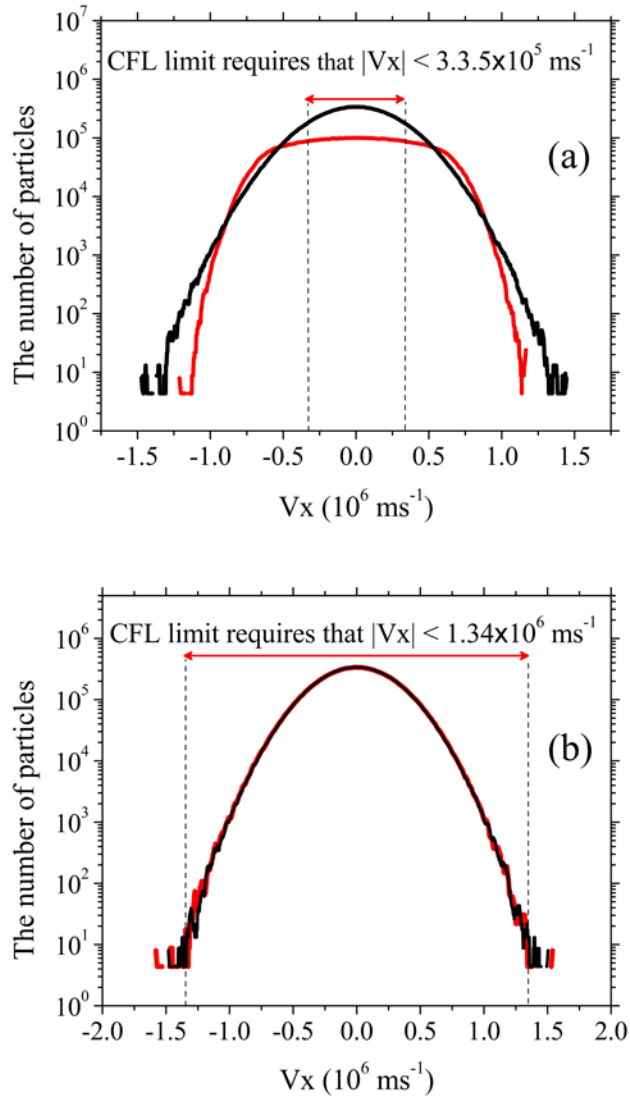


FIG. 9. V_x histograms with $2 \times 10^3 \text{ ms}^{-1}$ bins at $t = 0$, — , and at $t = 80 \text{ ps}$, — , for (a) the case W1 with $\Delta t = 20 \text{ ps}$, and (b) the case W2 with $\Delta t = 5 \text{ ps}$.

E. THE EFFECT OF MESH SIZE

Simulations were carried out on discrete mesh points. Their distribution had an effect on the simulations. To illustrate this, two mesh configurations were compared in simulation cases W2 and W3, whose parameters are listed in Table II. A cubic mesh was set up for the simulations. The mesh size at all three dimensions x, y (radial) and z (parallel to the magnetic field and the trap axis) were set to $6.7 \mu\text{m}$ in the case W2. The time step was 5 ps . After $1.6 \mu\text{s}$, wavelike variations appeared in the radial density profile as illustrated in Fig. 10(a) at $t = 3.2 \mu\text{s}$. These “density waves” remained in a constant position similar to a standing wave. To investigate the behaviors of these waves, the density histograms are fitted with the equation

$$n = K_1 + K_2 \exp(-K_3 R) \sin(K_4 R + K_5), \quad (5)$$

where K_1 is the mean density, K_2 is the amplitude, K_3 is the decay rate with radius, K_4 is the frequency in radial units, and K_5 is a phase shift. These coefficients are plotted in Fig. 11(a) versus time. The magnitude of K_4 remains constant (varies $\pm 2\%$) with time representing a wavelength of $7.52 \pm 0.15 \mu\text{m}$, which is close to the mesh size in the case W2, and so may suggest that the fluctuation of the radial density distribution inside the plasma may be due to the mesh size. To investigate this effect, the mesh size was reduced to $3.35 \mu\text{m}$ in the case W3 and the time step was reduced to $2.5 \mu\text{s}$ accordingly in order to avoid violating the CFL conditions, as $\Delta R / \Delta t = 1.34 \times 10^6 \text{ ms}^{-1}$. The "density wave" inside the plasma had the shorter wavelength of $3.38 \pm 0.05 \mu\text{m}$, which is in excellent accord with the smaller mesh size of $3.35 \mu\text{m}$ in the case W3. The value of K_4 in this case varied 1.5% as shown in Fig. 11(b). The magnitude of K_5 , which does not change effectively in both cases, implies the waves were fixed in radial position ($\pm 0.25 \mu\text{m}$) and so supports the idea of the waves dependency on the mesh size.

The values of K_2 and K_3 represent the amplitudes and decay rate of the density waves, respectively. The amplitude of the waves dropped by an order of magnitude when the mesh size was cut in half from 6.7 to $3.35 \mu\text{m}$. Furthermore, the density waves for the case W2 with larger amplitude was decayed by an order of magnitude faster with respect to the radius. Another coefficient, K_1 , the mean density in the wave region, oscillates three times larger in the case of larger mesh size, the case W2, compared to the case W1. The oscillation of the main density is caused by the radial oscillation of the plasma, which is seen by studying the plasma edge behavior in Fig. 12. The average radius of the plasma edge oscillates but does not increase within the current numerical uncertainty. Note that the width of the edge is oscillating much larger in the case W2 and that the case with smaller mesh size shows a harder plasma edge. The density profile smeared out further when the mesh size was increased. Using a smaller mesh size helped reduce both wavelength and amplitude of the density waves and lowered the plasma oscillation and prevents the generation of a high number of fast particles at the edge of the radial profile which in turn avoids high numerical noise. The radial position of the plasma edge at $t = 12 \mu\text{s}$ for the case W3 is also shown in Fig. 12. Comparing the values of average radius and the width of the plasma edge with the ones at $t = 4 \mu\text{s}$ and also noting that K_1 is constant, one proves that the plasma has not expanded anymore and shows a stable radius and edge width.

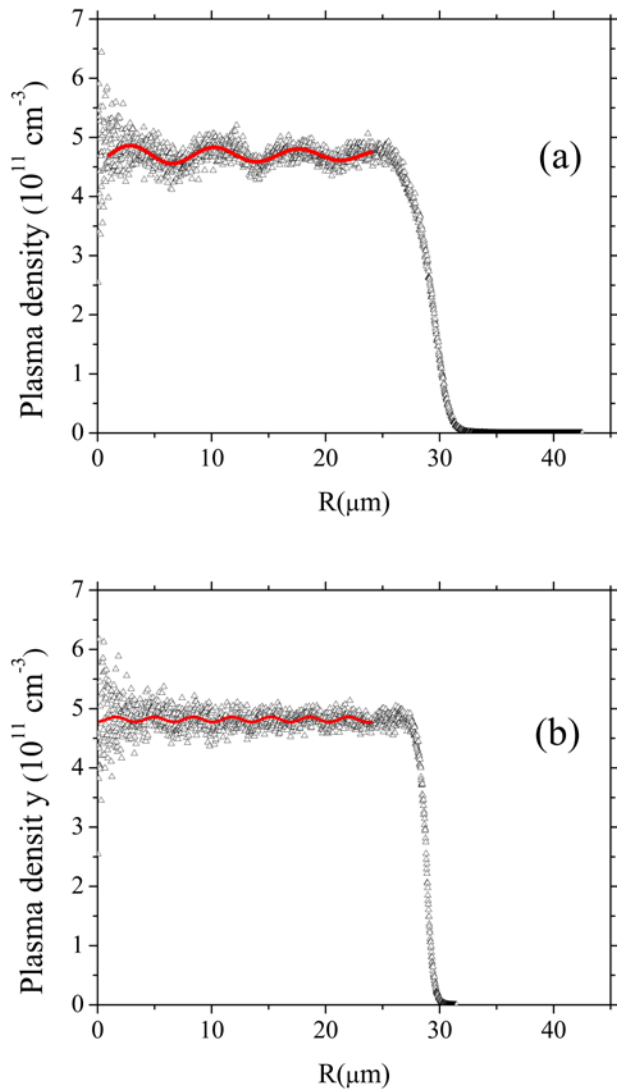


FIG. 10. The density histogram with $0.02 \mu\text{m}$ bins at $t = 3.2 \mu\text{s}$, Δ . Fit to data with Eq. (5), —, clearly shows the wavelike behavior for (a) the case W2 and (b) the case W3.

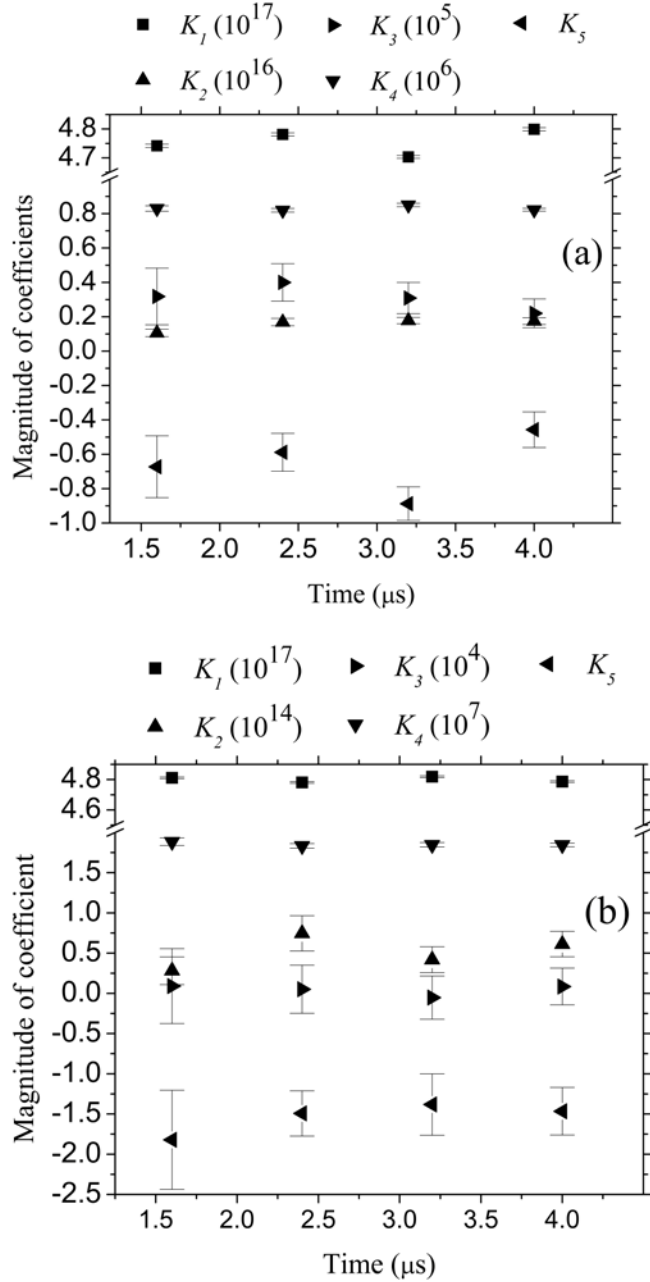


FIG. 11. The magnitude of coefficients versus time in the fitting Eq. (5) for (a) the case W2 and (b) the case W3. K_1 is the mean density, ■, K_2 is the amplitude, ▲, K_3 is the decay rate with radius, ▶, K_4 is the frequency in radial units, ▼, and K_5 is a phase shift, ◀.

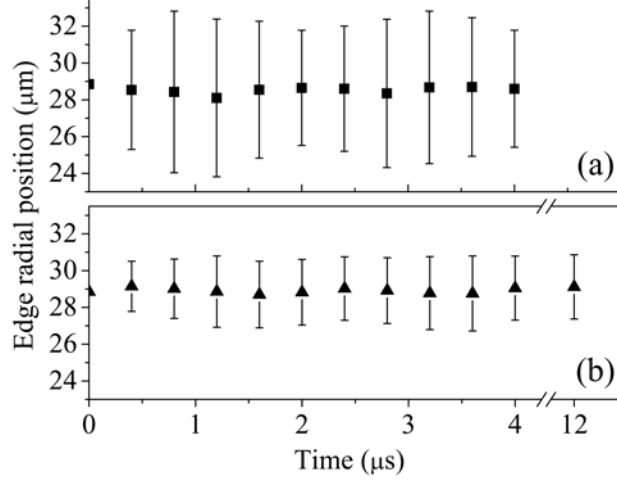


FIG. 12. The average radius of the tail versus time for a) the case W2, ■, and b) the case W3, ▲. The width of the plasma edge is shown as error bars.

F. TOWARD AN EQUILIBRIUM

All startup parameters are optimized so far in the case W3. If the plasma goes toward the equilibrium in which there is no transport across the magnetic field, the RMS of axial velocity (RMS V_z) should reach to a constant value. However, it has been shown [22] that there could be some oscillations in the RMS V_z value when a plasma nears the equilibrium in a PM trap. The RMS of axial velocity versus time for the case W3 is shown in Fig. 13. It increases with a rate that decays exponentially with time. Its initial value of $2.97 \times 10^5 \text{ ms}^{-1}$ would increase to $\sim 5.08 \times 10^5 \text{ ms}^{-1}$ at an equilibrium with the decay rate of 0.0344 (i.e. C_2^{-1} defined in Fig. 13) and with an asymptotic half-life of $20.1 \mu\text{s}$ (the time it takes to reach half way to the long run distribution). The velocity histograms at $t = 0 \mu\text{s}$ and $t = 12 \mu\text{s}$ in the case W3 are shown in Fig. 14. With time the axial velocity broadened while the radial distribution remained nearly constant. The kinetic energy histograms are fitted with Boltzman energy distribution function,

$$N = 2\sqrt{\frac{E_k}{\pi}} \left(\frac{1}{T(eV)}\right)^{3/2} \exp\left(-\frac{E_k}{T(eV)}\right) \quad (6)$$

Although the energy distribution is slowly varied from the Boltzman distribution near the equilibrium [15], it was still fitted acceptably with Boltzman distribution as plasma evolved toward higher temperatures as shown in Fig. 15(a). The inside graph implies that the temperature would increase to 0.895 eV at an equilibrium with the decay rate of 0.033 with an asymptotic half-life of $20.8 \mu\text{s}$, which is very close to the asymptotic half-life obtained from RMS V_z data, $20.1 \mu\text{s}$. These results along with what Fig. 12 implied that the case was nearing the equilibrium and numerical instabilities were unlikely to grow and dominate at larger timescales. Therefore, there was no need to run the simulation for longer times.

Experimental results showed [11, 24] increased loss rates of particles where the length of a trap was increased. However, with improvements in trap configuration such as a better alignment and

less variations of surface potential, the trapped particles survived longer. In the case W4, the influence of the length of the trap on the time to equilibrium was examined. Note that in the case W4 for the trap with 1 cm length grounded central tube, the plasma temperature increased to 0.576 eV with the decay rate of 0.236 as shown in Fig. 15(b) with an asymptotic half-life of 2.93 μ s. Therefore, the shorter the plasma we had, the faster the equilibrium it reached. Furthermore, the shorter plasma thermalized to a lower final energy.

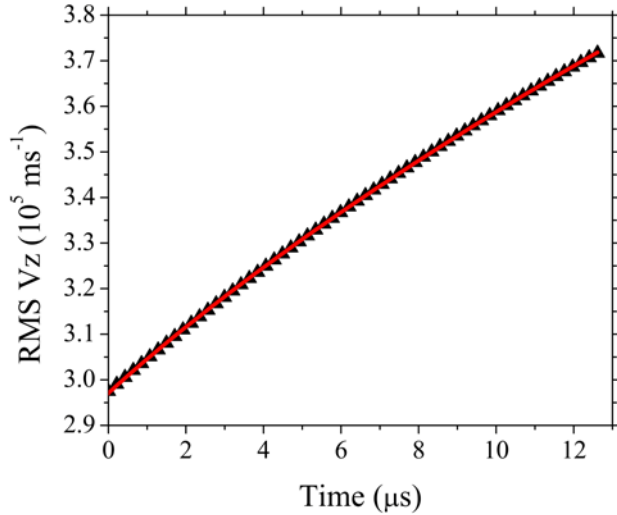


FIG. 13. The RMS V_z , \blacktriangle , versus time for the case W3. The fit to data, — , with $\text{RMS}V_z = C_1 \exp(-t / C_2) + C_3$ calculates $C_1 = -210434 \pm 62$, $C_2 = 29.01 \pm 0.01$, and $C_3 = 507899 \pm 63$.

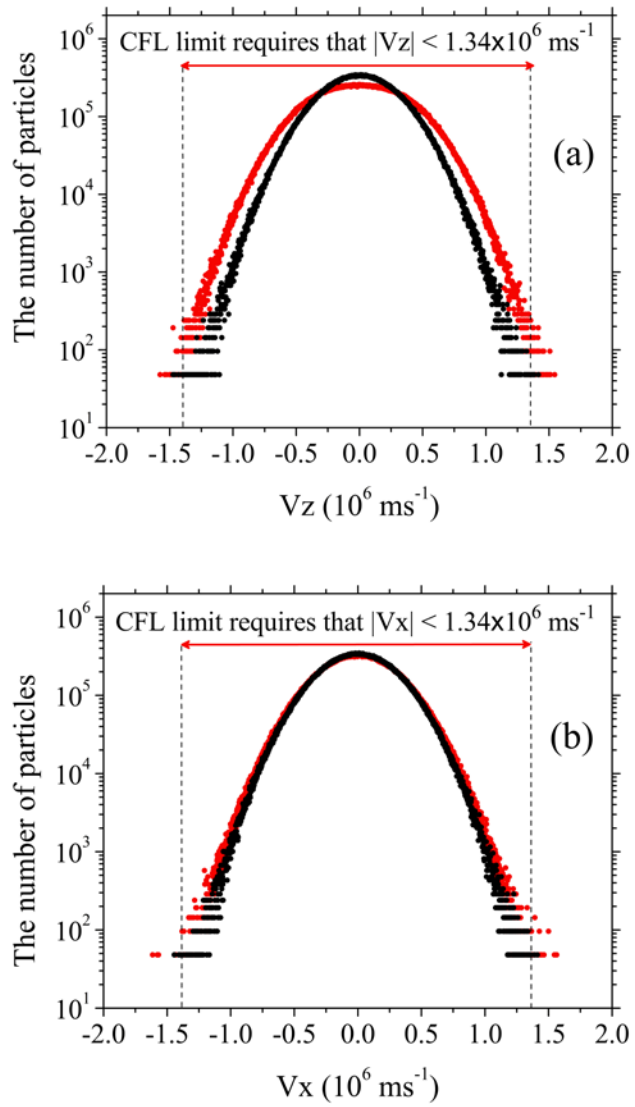


FIG. 14. (a) V_z and (b) V_x histograms with $2 \times 10^3 \text{ ms}^{-1}$ bins at $t = 0$, \bullet , and at $t = 12 \mu\text{s}$, \bullet , in the case W3.

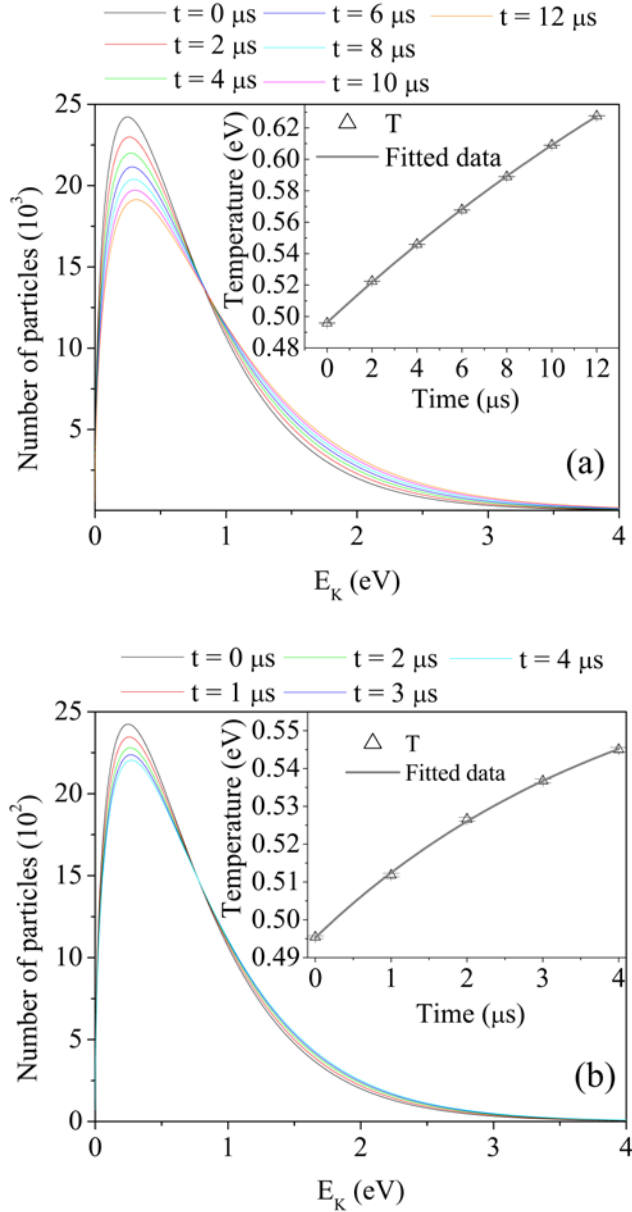


FIG. 15. Fitted date of kinetic energy histograms with Eq. (6), which calculates (a) $T_0 = 0.4958 \pm 1 \times 10^{-4}$, $T_{2\mu s} = 0.5224 \pm 1 \times 10^{-4}$, $T_{4\mu s} = 0.5459 \pm 1 \times 10^{-4}$, $T_{6\mu s} = 0.5679 \pm 2 \times 10^{-4}$, $T_{8\mu s} = 0.5889 \pm 2 \times 10^{-4}$, $T_{10\mu s} = 0.6090 \pm 2 \times 10^{-4}$, and $T_{12\mu s} = 0.6276 \pm 2 \times 10^{-4}$ for the case W3, and (b) $T_0 = 0.4954 \pm 4 \times 10^{-4}$, $T_{1\mu s} = 0.5118 \pm 5 \times 10^{-4}$, $T_{2\mu s} = 0.5266 \pm 5 \times 10^{-4}$, $T_{3\mu s} = 0.5367 \pm 5 \times 10^{-4}$, and $T_{4\mu s} = 0.5450 \pm 6 \times 10^{-4}$ for the case W4. The inside graphs show the plasma temperature versus time. The data is fitted with $T = F_1 \exp(-t / F_2) + F_3$, which calculates (a) $F_1 = -0.399 \pm 0.008$, $F_2 = 30.12 \pm 0.81$, and $F_3 = 0.895 \pm 0.008$ for the case W3, and (b) $F_1 = -0.0815 \pm 0.005$, $F_2 = 4.22 \pm 0.40$, and $F_3 = 0.576 \pm 0.005$ for the case W4.

While no particles were lost by reaching to the cylinder wall, about $2.9 \times 10^{-3}\%$ of particles escaped axially across the 10 V end electrodes in 12 μs in the case W3. The initial energy distribution of this case in Fig. 5 shows only $1.2 \times 10^{-3}\%$ of particles with kinetic energies more than 6.25 eV at the tail of the energy distribution. These positrons can imaginably pose total energies of more than 10 V if they fly near the axis in the plasma with 3.75 eV space charge potential on axis. Results showed that a higher percent of particles ($2.9 \times 10^{-3}\%$) escaped from the end caps of 10 V potential in this case. The particles loss rate is increasing, as shown in Fig. 16, which is caused by the numerical heating in the simulation. Figure 17 illustrates that most of these particles were lost close to the central axis of the trap where the space charge potential were maximum for the symmetric plasma. So the lost was not due to the outward drift which causes kinetic energy to increase. The solution to get rid of this instability was found at choosing smaller positron weight. The case W5 assembled all the parameters in case W3 but the positron weight of almost 10 times smaller. This case was modeled for the trap with 5 mm length grounded central tube to avoid very high computational times as if we would keep the same length of 10 cm, it would cost couple of months computing on the same computational hardware on the high performance computer. Simulation result showed that $2.4 \times 10^{-4}\%$ of particles were lost (only 3 macro-particles) in the case W5 after 10 μs .

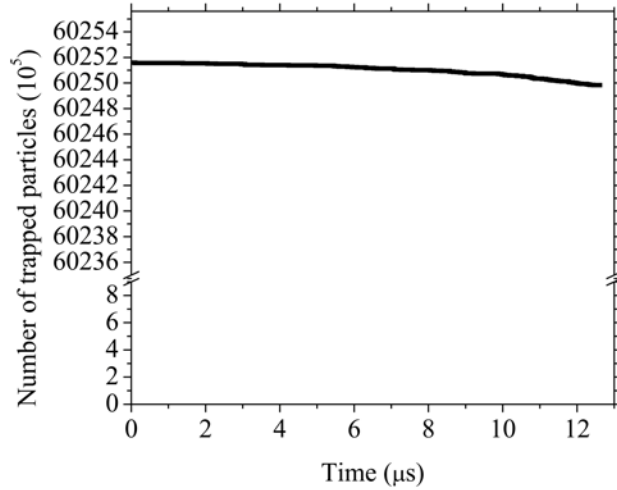


FIG. 16. The number of trapped particles versus time in the case W3.

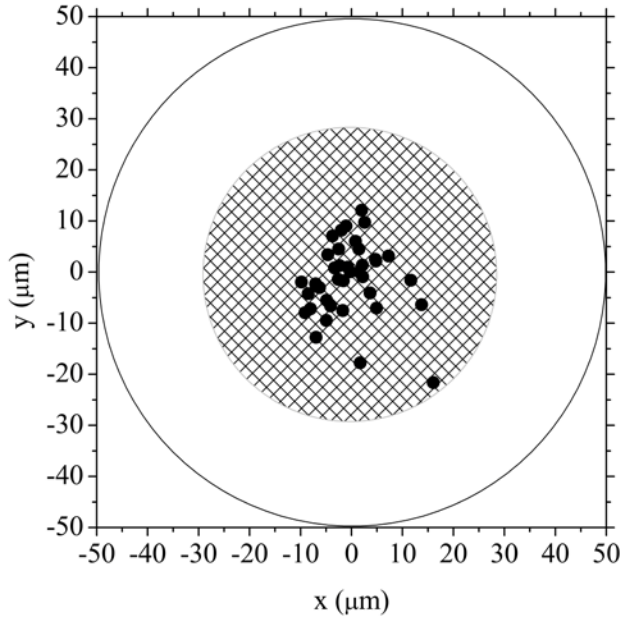


FIG. 17. The cross section of one end cap shows the position of the lost particles, \bullet . The patterned surface represents the initial plasma.

G. MAXIMUM FINAL DENSITY

We have studied so far the behavior of a plasma with 3.75 V space charge potential on axis. One would also like to know what the highest density of positrons is that can be trapped in the 50 μm radius microtrap with the 10 V end barriers. In order to investigate this, the microtrap was filled up initially with a uniform plasma of ten times higher density and a space charge of 37.5 V on axis in the case W6. For example, suppose that the end cap potentials were much higher at the first, similar to what we will show in section H, enabled us to fill the microtrap up to this initial density. Then the barriers potentials were dropped to 10 V. Lowering the end cap potentials is a well known technique to manipulate a desirable plasma with narrow energy character [25]. It is predictable that end electrodes of 10 V potential were not able to trap this high space charge plasma and particles started to escape from end caps until a confineable density was reached. Figure 18(a) shows the trapped particles versus time in the case W6. The inner graph is a zoomed in view in which the data is fitted with third order exponential decay function. The data fits this asymptotic function well and 36.82% of initial particles were trapped at the equilibrium. The higher energy particles at the tail of the Boltzman energy distribution escaped from the end caps at the initial stages of simulation which caused dropping the space charge potential. It was moreover seen, as shown in Fig. 19, that the plasma was evolved in density distribution while it presented consistent distribution after 0.5 μs . The plasma is not uniform anymore because the particles were more lost close to the axis where the space charge potential was highest. Hence, the density was significantly dropped at the axis. The potential along the plasma axis was

reached to about 9.3 V after 2 μ s as shown in Fig. 20, which was confined by 10 V end cap potentials.

By solving the Poisson's equation, $\nabla^2\varphi = -\frac{\rho}{\epsilon}$, the electrostatic potential, φ , was calculated with respect to the radius at $t = 2 \mu$ s in Fig. 21 from the charge density, ρ , in Fig. 19. It was seen that the evolved density distribution, which was not uniform anymore, corresponded to a relatively constant potential along the radius of the plasma, close to 9.32 V. The end electrodes of 10 V were capable to confine the rest of the particles axially in the microtrap after this distribution was reached. Evaporation of high energy particles leads to creation of a narrower energy plasma, illustrated in Fig. 22.

The densities at the cases W7 and W8 were initialized two and four times higher, respectively, compared to the case W6. We observed that even higher numbers of particles were trapped in these cases, as illustrated in Fig. 18. The plasma potential at 2 μ s, as shown in Fig. 23, increased with initial space charge on axis. Note that the plasma with highest initial density smeared out further to about 34 μ m radius. The inner graph predicts that maximum density of $7.21 \times 10^{11} \text{ cm}^{-3}$ is achievable in one microtrap of 50 μ m radius and 10 V barriers potential, which corresponds to the axial space charge potential close to 9.98 V.

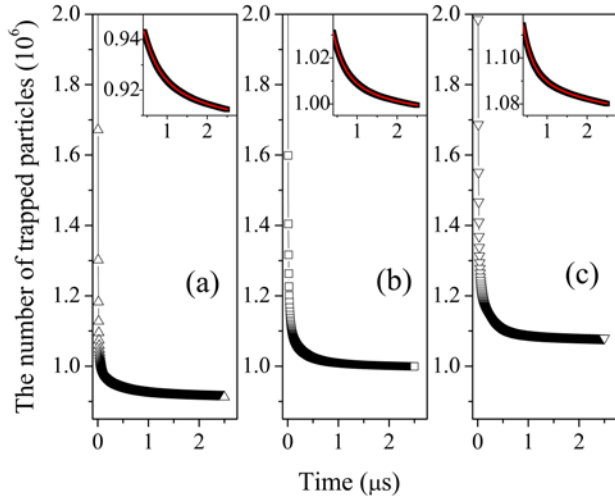


FIG. 18. The trapped particles versus time in a) the case W6, b) the case W7, and c) the case W8. The inner graphs are zoomed in view. The data are fitted, — , with third order exponential decay function. 36.82%, 20.20% and 10.90% of initial particles were trapped at the equilibrium, respectively, corresponding to densities of 5.89×10^{11} , 6.46×10^{11} and $6.97 \times 10^{11} \text{ cm}^{-3}$ in one microtrap.

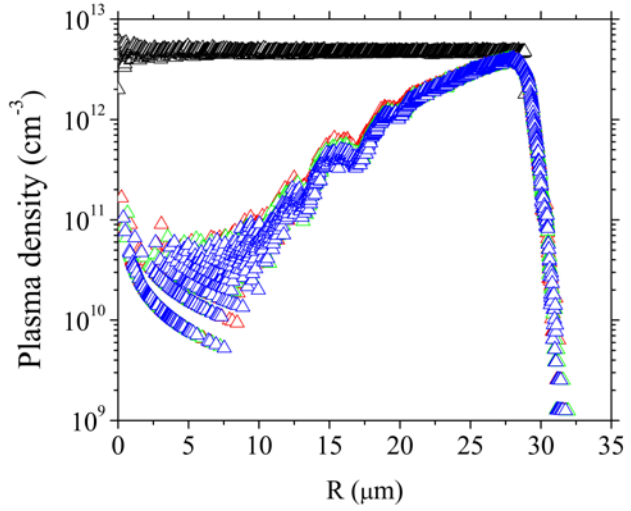


FIG. 19. The density histogram with $0.02 \mu\text{m}$ bins at $t = 0 \mu\text{s}$, Δ , at $t = 0.5 \mu\text{s}$, Δ , at $t = 1 \mu\text{s}$, Δ , and at $t = 2 \mu\text{s}$, Δ , in the case W6.

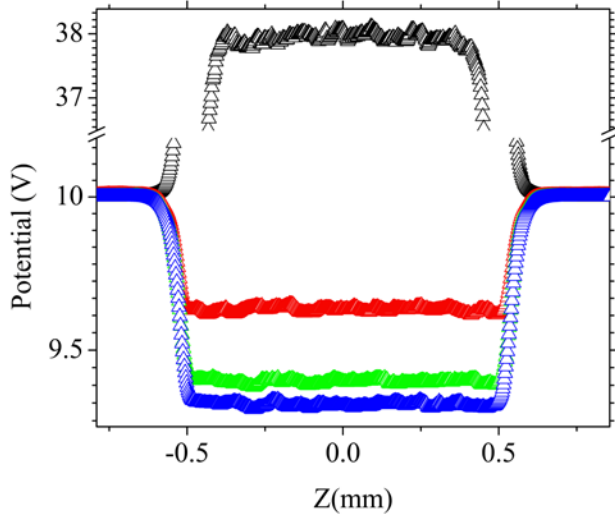


FIG. 20. The potential along the axis of the microrap (main tube extends from $z = -0.5$ to 0.5 mm) at $t = 0 \mu\text{s}$, Δ , at $t = 0.5 \mu\text{s}$, Δ , at $t = 1 \mu\text{s}$, Δ , and at $t = 2 \mu\text{s}$, Δ , in the case W6.

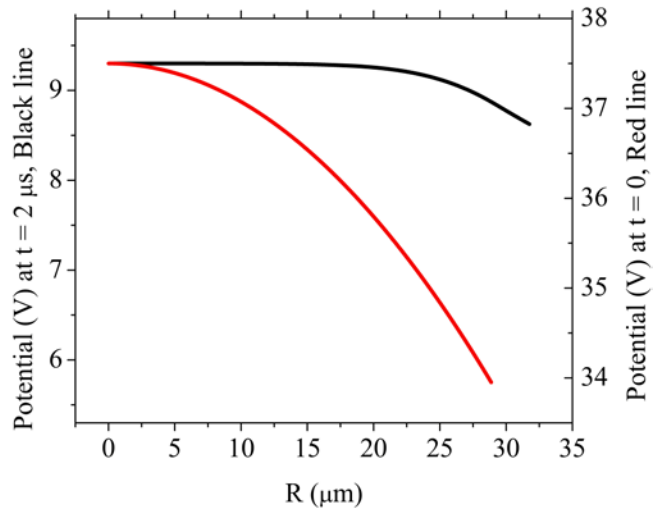


FIG. 21. The potential versus radius at $t = 0 \mu\text{s}$, —, and at $t = 2 \mu\text{s}$, —, in the case W6.

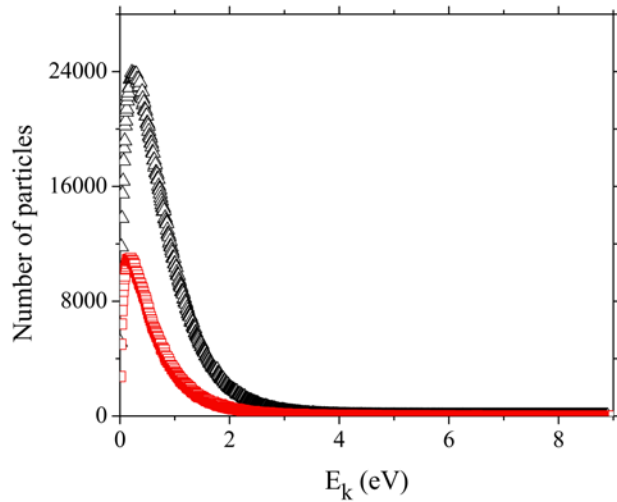


FIG. 22. Kinetic energy histogram of the plasma at the case W6 with $1 \times 10^{-2} \text{ eV}$ bins, at $t = 0 \mu\text{s}$, Δ , and at $t = 2 \mu\text{s}$, \square . Evaporation of high energy particles due to lowering the end cap potentials leads to manipulate a plasma with narrower energy.

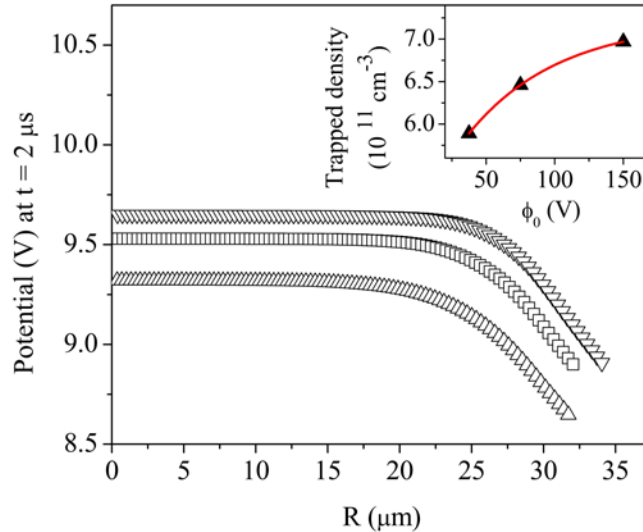


FIG. 23. The potential versus radius at $t = 2 \mu\text{s}$, when initial space charge potential on axis was equal to 37.5 V, Δ , 75 V, \square , and 150 V, ∇ . Inner graph shows the final trapped density versus the initial space charge potential on axis, which exhibits an asymptote equal to $7.21 \times 10^{11} \text{ cm}^{-3}$ of density.

H. HIGHER END ELECTRODES POTENTIAL

We can easily increase the barriers potential up to one order of magnitude higher than 10 V and still we have a quite portable trap. We simulated the case W9 with parameters consistent to the case W6 but the end electrodes potential of 50 V. The simulation resulted in a uniform plasma with a soft edge similar to the case W3. No clear density waves were seen, as shown in Fig. 24, which were previously appeared in the lower density plasma in the case W3. The reason is the fact that we had a 10 times higher number of macro-particles per cell in modeling of the case W9 compared to the case W3. Figure 25 illustrates the values of average radius and the width of the plasma edge at $t = 0.5 \mu\text{s}$ and at $t = 1 \mu\text{s}$. It proves that the plasma did not expand anymore after $0.5 \mu\text{s}$ and showed a stable radius and edge width. The plasma experienced a loss rate which was decelerating exponentially as shown in Fig. 26. The data is fitted well with a third order exponential decay function, representing that the $2.5 \times 10^{-4}\%$ of initial particles would be lost in total at the final equilibrium.

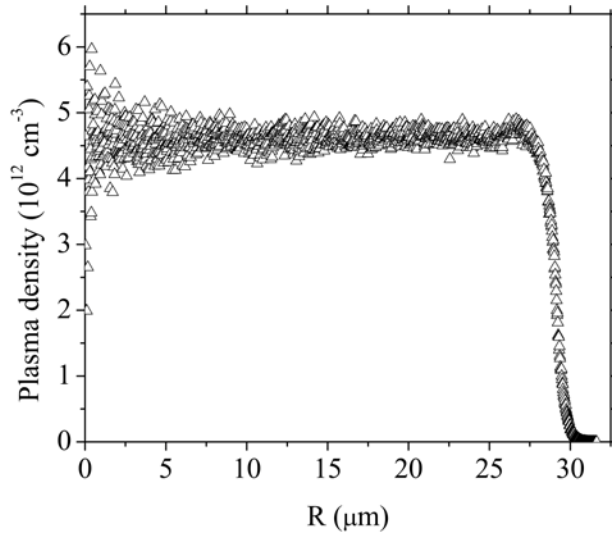


FIG. 24. The density histogram with $0.02 \mu\text{m}$ bins at $t = 1 \mu\text{s}$, Δ , in the case W9.

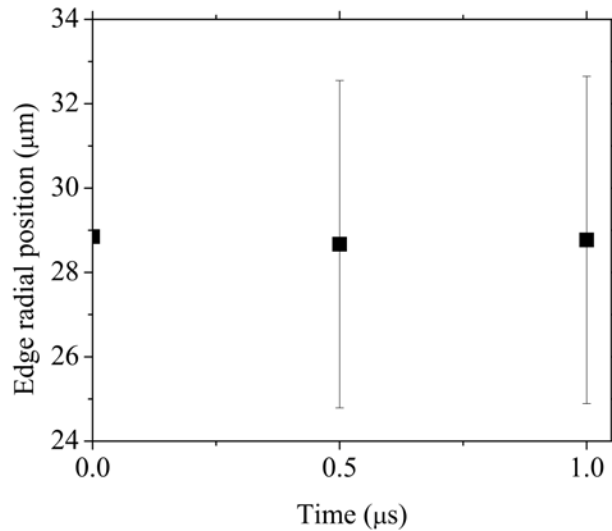


FIG. 25. The average radius of the tail versus time for the case W9, ■. The width of the plasma edge is shown as error bars.

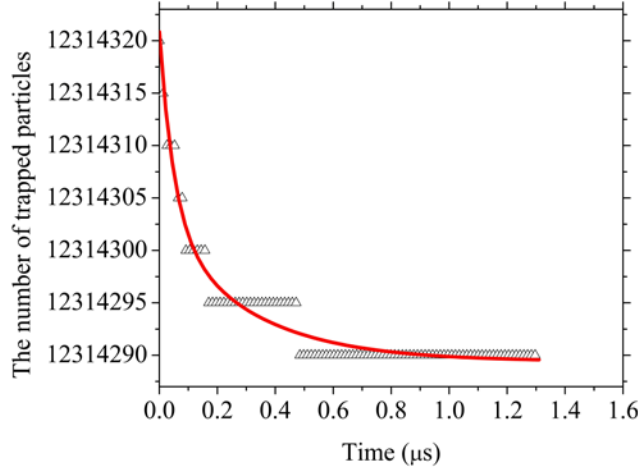


FIG. 26. The trapped particles versus time in the case W9, Δ . Each dropping step corresponds to one macro-particle lost. The data is fitted, —, with third order exponential decay function.

The analytical expectation from Eq. (3) shown in Fig. 4 is shifted up when the space charge is increased to 37.5 V, suggesting that the Brillouin limit may be surpassed at 3 μm radius microtrap, as shown in Fig. 27, while the end caps potential is only 50 V.

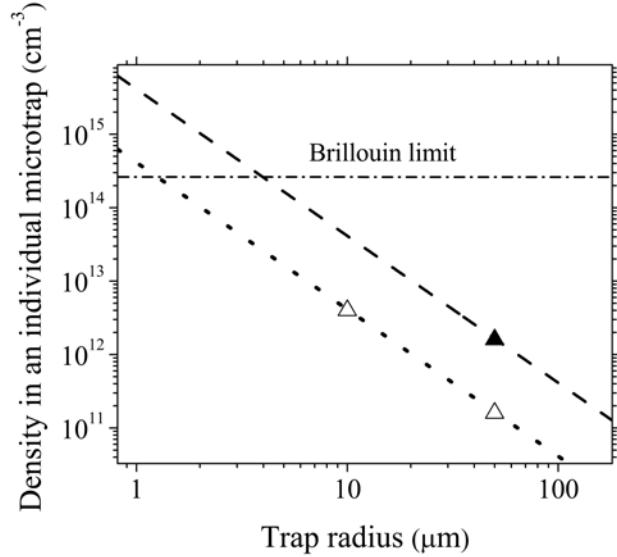


FIG. 27. The density of the plasma as a function of the radius of the microtrap when $R_w/R_p = \sqrt{3}$. The analytical expectations from Eq. (3) are shown when the initial space charge is 3.75 V and end caps potential is 10 V, the dot line, and when the initial space charge is 37.5 V and end caps potential is 50 V, the dashed line. The cases W5 and W11 results, Δ , in which the

initial space charge was 3.75 V and end caps potential was 10 V, and the case W9 result, \blacktriangle , in which the initial space charge was 37.5 V and end caps potential was 50 V.

IV. DESCRIPTION AND RESULTS OF WARP SIMULATION OF THE 10 μm RADIUS MICROTRAP

In order to simulate 10 μm radius microtrap, we scaled down the parameters of the case W3; in the case W10, the mesh size is five times smaller, 0.67 μm . While the initial temperature of the plasma was kept the same, 0.5 eV, the time step experienced the same reduction as the mesh size, which was 0.5 ps. The initial energy distribution was a Boltzmann distribution. As we discussed earlier, the modeling trap length was chosen shorter as we go to smaller diameters to keep the aspect ratio small. The main tube length was chosen equal to 5 mm at the case W10. The initial length of the plasma is 4.998 mm with the cigar shape ends. In order to keep the initial number of macro-particles per mesh cube cell bigger than $\frac{1}{3}$, similar to the case W3, the positron weight

was decreased from 48 to 9. CFL condition is violated when the velocity of the particle exceeds $\Delta R/\Delta t = 1.34 \times 10^6 \text{ ms}^{-1}$. Figure 28 illustrates that although that the initial simulation parameters were chosen in a way that no particles were violated the CFL condition at $t = 0$, more than 0.48% of particles after 3 μs showed higher velocities than the limit. The plasma smeared out due to the numerical heating. Figure 29(a) illustrates while the average radius of the plasma tail remained constant after 1 μs , the tail width was still expanding after 3 μs in the case W10. Relatively high amount of particles, 3%, was lost at the end electrodes in this case after 3 μs due to the high numerical instabilities and the lost rate were accelerating as shown in Fig. 30.

Similar to 50 μm radius microtrap, the instability was avoided by choosing smaller positron weight at the case W11. The case W11 assembled all the parameters in case W10 but the positron weight of 9 times smaller, equal to 1. The average radius of the plasma tail and the tail width remained constant after 0.25 μs , as shown in Fig. 29(b). Figure 31 illustrates the trapped particles versus time in both cases W10 and W11. The 99.98% of initial particles in the case W11 were trapped at the final equilibrium.

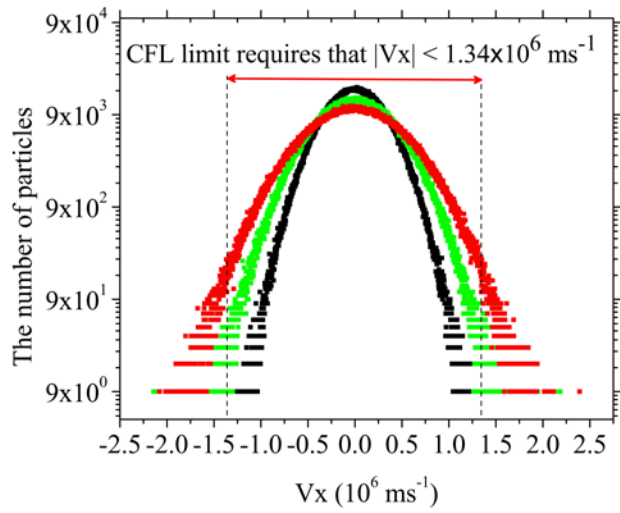


FIG. 28. V_x histogram with $2 \times 10^3 \text{ ms}^{-1}$ bins at $t = 0$, ●, at $t = 1$, ●, and at $t = 3 \mu\text{s}$, ●, in the case W10.

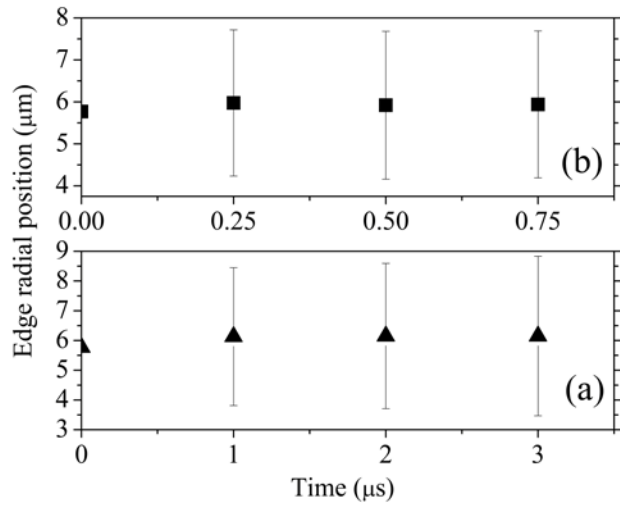


FIG. 29. The average radius of the tail versus time for a) the case W10, ▲, and b) the case W11, ■. The width of the plasma edge is shown as error bars.

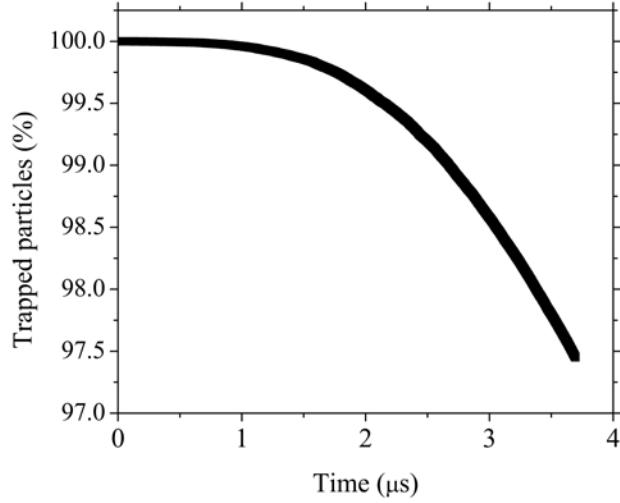


FIG. 30. The trapped particles versus time in the case W10.

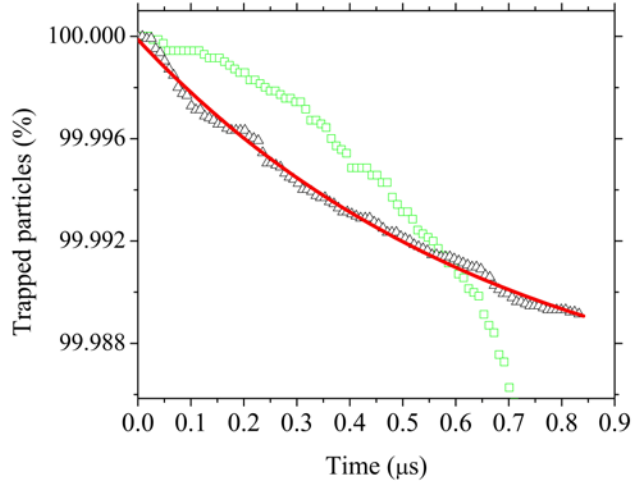


FIG. 31. The trapped particles versus time in the case W10, Δ , and in the case W11, Δ . The case W11 data is fitted, $\textcolor{red}{—}$, with a third order exponential decay function.

V. CPO

The CPO program was used to investigate the trajectories of positrons in the proposed microtrap. It uses single charge particle optics and includes space charge effects. This program uses the 'Boundary Element Method' or 'Surface Charge Method' to obtain the potential and fields at any point. CPO can incorporate space charge either by the 'space-charge cell' method or by the 'space-charge tube' method, which follow the path of select particles. The program distributes the desired charge uniformly in each cell or tube. The 'tube' method is primarily intended for simulations involving long thin beams. With the 'cell' method an accurate treatment might

require that the cell dimension be too much short [18]. For long thin beams the creation of a large number of cells is undesirable compared to a small number of tubes used in the 'tube' method. In the present simulations, the 'space-charge tube' method is used. Each ray represents a specific number of charged particles. The number of rays is limited by the length of the ray paths and the magnitude of the step time. A larger number results in more homogeneous space charge distributions. Forty-nine and sixty-four space charge tube rays were applied for the short simulations (cases S6-S8). The space charge tube diameter was set to recommended one quarter of the microtrap radius [18]. Each iteration is defined as a complete loop in which the rays fly one time back and forth in whole length of the trap. The code uses several iterations by applying the space charge of the current iteration upon the rays for the next iteration. The motion of the charged particles was traced by investigating the trajectories of a number of rays.

For the short simulations, all rays initialized parallel to the axis of the microtrap at the center of the microtrap on a vertical middle plane. Each ray completed an iteration and ended at the same middle plane. A loop program using the C⁺⁺ language was used to setup the initial conditions of each ray in one iteration based on the final conditions of all the rays in previous iterations. If more than one ray is used, the rays are started uniformly with the same kinetic energies. This is a large simplification because the CPO program does not read in the initial conditions of all rays and each individual ray cannot be traced correctly through all iterations. At every iteration all rays were distributed within a circle. The radius of this circle and the energy of the rays were calculated from the average final radii and energies for the last iteration. As simulation progressed, some of the rays hit the microtrap wall and were lost. This process continued until the space charge decreased to a value that rays would no longer be lost. Then, the number of trapped particles was calculated as the flight time of the remaining rays multiplied by the total current of the rays. All the short simulations based on the explained procedure are listed in Table III.

For the microtrap of 50 μm radius, a different method was used to obtain more accurate results. The parameters used in this simulation are listed in Table III. One ray was flown along the axis of the trap from one end of the central tube to the other end, which produced a uniform cylindrical hard edge charge cloud with the radius equal to $R_w/\sqrt{3}$ (Space charge tube diameter, $SCTD = 2R_w/\sqrt{3} = 57.7 \mu\text{m}$). This is the space charge due to the predetermined number of positrons in the trap. Individual rays were subsequently flown within this uniform, constant space charge and their trajectories were traced. The improvement of this method over that discussed above, used to obtain the short runs results presented in Fig. 4, is that each ray was traced correctly and without discrete iterations. In a uniform cylindrical plasma, a particle at the cloud edge experiences highest electric field. It was assumed that if one ray was flown near the cloud edge, which in our cases was radius of 28.82 μm , and did not expand in time, the whole particles would stay together without expansion. Therefore, the pre-established charge was trapped.

In CPO, it was necessary to specify a time step that was shorter than the gyro period; otherwise, the trajectory integration routine did not give accurate results. The CPO routine uses the Bulirsch-Stoer method and a time step equal to the gyro period is insufficient [18]. To investigate the effect of step time, a plasma was established, as described above, with radius 28.85 μm and an axial space charge potential 4.5 V, in which a positron was flown at a radius 28.80 μm with

$V_z = 1.32 \times 10^6 \text{ ms}^{-1}$ within the central length of the microtrap. For example, when a 5 ps time step was chosen, this positron lost 99% of its axial velocity, which was transferred to radial velocity due to the numerical inaccuracies, within 100 ns. To obtain the correct helical motion, the time step must be less than 0.4 ps in the case of a 7 T magnetic field. Figure 32 shows the trajectory of a particle in presence of a uniform cloud at the cloud edge within the central length of the microtrap for time steps of 0.4 and 0.8 ps. The data are fitted with equation $R(\&V_{\perp}) = P_1 + P_2 \sin(P_3 t + P_4)$. While the mean transverse velocities for the cases with time steps of 0.4 ps and 0.8 ps were $4.9 \times 10^4 \text{ ms}^{-1}$ and $1.94 \times 10^4 \text{ ms}^{-1}$, respectively, the gyro radius, r , was obtained from

$$r = \frac{mV_{\perp}}{q|\vec{B}|}, \quad (7)$$

where V_{\perp} denotes the transverse velocity, resulting in radii of 39.6 nm and 15.74 nm for 0.4 ps and 0.8 ps, respectively. The CPO simulated the radii of 39.51 nm and 5.50 nm for these two cases consequently, maintaining 99.4% and 34.9% accuracy for the 0.4 ps case and the 0.8 ps case in the order given. Note that the radius of the gyro-center, P_1 , in the 0.4 ps case was smaller than the case with 0.8 ps step time. While the initial radius of the positron was 28.80 μm , it implies that the positron in the case with larger step time experienced 5 times higher expansion rate. Simulation resulted in a gyro period, $2\pi/P_3$, equal to 6.4 ps and 6.8 ps using step times 0.4 ps and 0.8 ps, respectively.

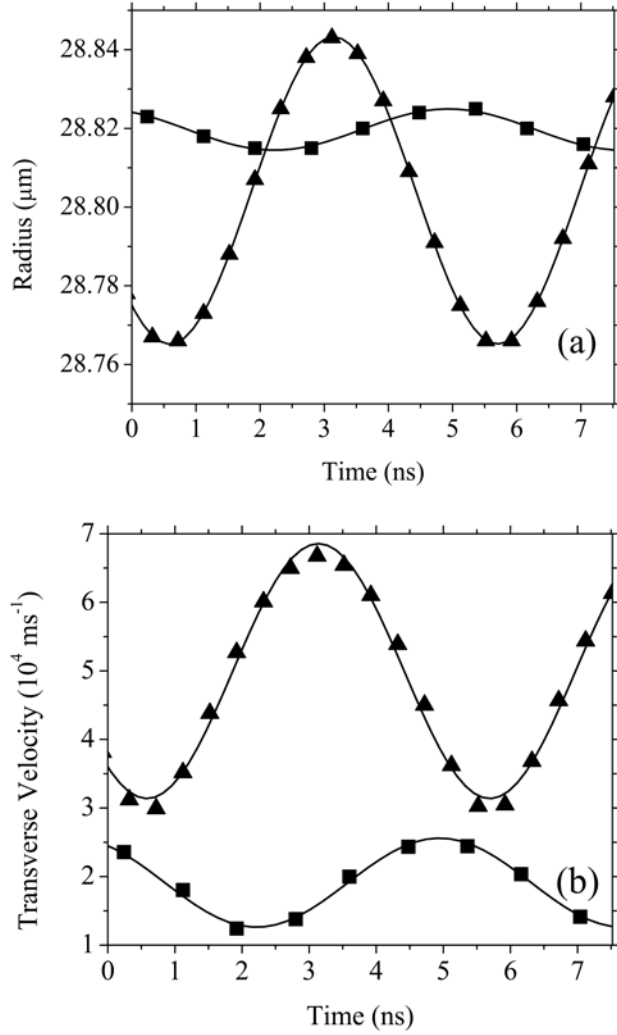


FIG. 32. Trajectory of a positron flying at the edge of the uniform plasma with 4.5 V of axial space charge potential with two different time steps, 0.4 ps, Δ , and 0.8ps, \blacksquare . The data are fitted with equation $R(\&V_{\perp}) = P_1 + P_2 \sin(P_3 t + P_4)$. (a) The radius data calculates $P_1 = 28.80424 \pm 0.00007$, $P_2 = 0.03901 \pm 0.0001$, $P_3 = 982.82 \pm 0.86$, and $P_4 = -2.295 \pm 0.005$ when step time is 0.4 ps (Δ), and calculates $P_1 = 28.81972 \pm 0.00012$, $P_2 = 0.00524 \pm 0.00016$, $P_3 = 926.81 \pm 8.52$, and $P_4 = -4.146 \pm 0.039$ when step time is 0.8 ps (\blacksquare). (b) The transverse velocity data calculates $P_1 = 19113.29 \pm 159.58$, $P_2 = -6494.84 \pm 212.43$, $P_3 = 983.94 \pm 8.12$, and $P_4 = -0.9760 \pm 0.0419$ when step time is 0.4 ps (Δ), and calculates $P_1 = 49976.49 \pm 320.43$, $P_2 = 18599.83 \pm 443.48$, $P_3 = 920.54 \pm 9.03$, and $P_4 = -2.2892 \pm 0.0472$ when step time is 0.8 ps (\blacksquare).

For a plasma with 0.5 eV temperature, the majority of particles have kinetic energy less than few eV. Since it can also be assumed that, initially, the most energetic particles are more likely to expand, a particle with 5 eV kinetic energy was chosen in CPO simulations.

Different gap sizes between grounded central tube and end electrodes were studied while in the gap region it was defined either a linearly changed voltage electrode, or overlapped electrodes of different radii and overlapping sizes, or even no electrode. The results from CPO were not consistent when the parameters of the end electrodes and gaps were slightly varied. Another problem of modeling end electrodes was that as the ray comes near the end cap it slows down, stops and then returns on axis while the program assigns a charge q uniformly distributed along the step line, where $q = I \times \Delta t$. So the space charge was deposited uniformly on time steps, causing high space charge accumulation near the end caps, which was highest at the turning point. The positrons which entered that high potential were bounced back. In order to simplify the simulation for a microtrap which has a high aspect ratio, we assume that the particle flies within an infinitely long microtrap. In the interest of study the effect of the space charge on the trajectory of one positron that is not affected by the end electrodes, a shell C++ program was written to make the particle travel back and forth within the central region of the modeled microtrap. It stopped the particle when it reached a x-y plane located 5 mm away from each end cap, recorded the data and reinitialized the particle with the same parameters but opposite axial velocity. Three cases (C1, C2 and C3) with cylindrical, uniform plasmas, of radius 28.85 μm and axial space charge potentials of 0.375, 1 and 3.75 V were simulated in the 50 μm radius microtrap. One particle was flown in presence of each space charge, with an initial radius of 28.82 μm at the plasma edge. The particle was initialized with a kinetic energy of 5 eV and no transverse velocity. Figure 33 shows the radius for the particle of each case versus time. Note that the particle expanded at an almost constant rate in each individual case. The expansion rates showed that the maximum space charge among these cases where the radius of the guiding center of the particle was almost constant was 1 V in the case C2. The particle at the edge of a space charge cloud, which experienced the highest repulsive electric field, did not move out radially if the space charge potential on the axis of the cloud was 1 V or less. At the higher density there was a clear expansion as expected.

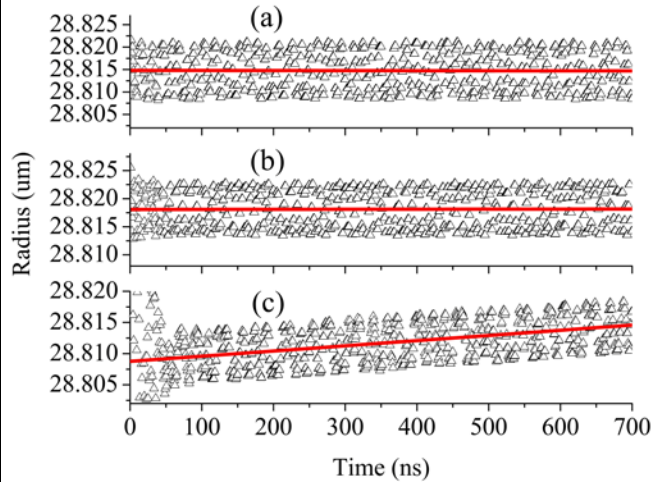


FIG. 33. Radius of the positron flying in presence of the uniform hard edge plasma with $28.85 \mu\text{m}$ radius and the axial space charge potential of (a) 0.375 V in the case C1, (b) 1 V in the case C2, and (c) 3.75 V in the case C3. The initial radius of the positron is $28.82 \mu\text{m}$. The data are fitted with linear function, —, which calculates radius change rate of -0.13 ± 0.60 for the case C1 with $\varphi_0 = 0.375 \text{ V}$, 0.08 ± 0.46 for the case C2 with $\varphi_0 = 1 \text{ V}$, and 6.92 ± 0.3 for the case C3 with $\varphi_0 = 3.75 \text{ V}$.

IV. DISCUSSION

WARP results agreed well with the predictions from a simple analytic expression. The density was proportional to the inverse square of the trap radius. Short simulations produced results that agreed quite well with long term more precise more elaborate calculations in WARP. The difference was about 35%. The additional computational effort for the extra 35% was tremendous, including about 15 times stronger computational hardware with 10 times higher simulation time. CPO results deviated dramatically and the trapped density followed more a R_W^{-1} dependence.

We discussed how to reduce the numerical noise in WARP simulations by optimizing modeling parameters to obtain the equilibrium for non-neutral plasmas within a microrap with $50 \mu\text{m}$ radius. An experimental effort is under way to store positrons in $50 \mu\text{m}$ radius, 100 mm long traps in a uniform axial field of 7 T . Experimental and modeling results will be compared. It was shown that choosing sufficiently small values of time step and mesh size avoids the plasma heating in the WARP simulations. The density profile smeared out further when the mesh size was increased. The case with improved parameters, case W3, presented a steady radial density profile after $12 \mu\text{s}$ and the equilibrium was expected to reach in approximately $180 \mu\text{s}$. The velocity distribution at the equilibrium evolved but remained in the CFL limits. The positron weight was also optimized in the case W5, helped to omit the numerical heating caused particles to escape from end caps. The significance of this study relies on the fact that it is given that even the initial plasma distribution with cigar shape ends is far from the idealized equilibrium, the proposed model does result in the computational equilibrium, while the hard edge plasma

evolved to the soft edge. The width of this soft edge does not change and is equal to $1.75\text{ }\mu\text{m}$ when the plasma is near the equilibrium.

It was shown that as the plasma expanded and evolved toward the soft edge distribution, the electrostatic energy of the space charge decreases and it is converted into kinetic energy which is called Joule heating. The shorter plasma was found to reach to a lower temperature at the equilibrium. This heating effect can be partially compensated by the resistive cooling mechanism which is significant in micro scales and can be a subject of future simulations. However, the cyclotron radiation cooling mechanisms is inhibited in our scale due to the high cut frequency of the microtrap as a waveguide.

It was demonstrated computationally by WARP code that a uniform, soft edge plasma with density of $1.6 \times 10^{11}\text{ cm}^{-3}$ can be trapped in one microtrap with the radius of $50\text{ }\mu\text{m}$ and confining potentials of 10 V ; hence 2.35×10^{13} positrons can be trapped in an array of 187,500 microtraps filling the size of a soda can (5 cm diameter and 10 cm length), assuming that the filling factor is 75%. This density is comparable to the highest reported density in a conventional Penning-Malmberg trap ($\approx 10^{11}\text{ cm}^{-3}$) which uses order of kV electrostatic potentials and often some means such as rotating walls to confine the plasma radially because of the high existing space charge and outward electric forces. Ten times higher density was trapped when barrier potentials was increased to 50 V , suggesting that the Brillouin limit may be surpassed at $3\text{ }\mu\text{m}$ radius microtrap.

The maximum trapped density in one microtrap of $50\text{ }\mu\text{m}$ radius and 10 V end cap potentials was found to be even about 3 times higher than stated above, which was achieved by putting about one order of magnitude higher number of particles initially and lowering the end cap potentials to 10 V then. However, the final density distribution was not uniform anymore.

CPO applies to the single particle regime and so does not include collisions between the particles. Furthermore, the results from CPO were not consistent when the parameters of the end electrodes and gaps were slightly varied. High space charge accumulation near the end caps was seen. Therefore, the results from this tool should be considered with caution. If the particle is low enough in energy so that it can be confined axially (e.g. a 5 eV kinetic energy particle in a plasma of 3.75 V space charge potential and a microtrap with 10 V end electrodes) one can follow the trajectory of the particle using CPO program while the end cap issues are avoided. For the case of $50\text{ }\mu\text{m}$ radius traps, the corresponding density was less than a third of the density achieved with WARP. Considering the limitations of the CPO, accuracy of the results especially near the end electrodes region, and also capabilities of this program to simulate in a plasma regime, the CPO is not suitable for modeling the plasmas in PM traps or similar systems.

Simulations will be extended to smaller radius traps where the simple analytic prediction crosses the Brillouin limit. We will also try to figure out what trap radius and what aspect ratio is ideal for storing large number of particles in practice. Experimental efforts to test the long aspect ratio microtrap array are under way. Losses arise on experiments by patch effects, annihilation with gas molecules, and by trap imperfections such as nonalignment of microtraps, asymmetries, and non uniform magnetic field. Simulations will also help to investigate these effects and find out the amount of deviations from perfectness which is tolerable in our design. Computational studies might also be required for the positron transport and injection into the trap.

V. ACKNOWLEDGEMENT

The authors are grateful to colleagues at WSU, Paola Folegati for her contribution to the early stages of the project, and Randall Svancara for his helps to the simulations on HPC. We are also thankful to Dr. David Grote at LLNL for assistance and useful discussions regarding the WARP simulations, and also Dr. Frank Read for his helps toward CPO simulations. We would also like to thank program managers Dr. William Beck and Dr. Parvez Uppal of the Army Research Laboratory who provide funding under contract W9113M-09-C-0075, Positron Storage for Space and Missile Defense Applications, and program manager Dr. Scott Coombe of the Office of Naval Research who provide finding under award #N00014-10-1-0543, Micro- and Nano-Traps to Store Large Numbers of Positron Particles at Very Large Densities.

1. D. B. Cassidy and A. P. Mills, Jr., *Nature* 449, 195 (2007).
2. R. G. Greaves and C.M. Surko, *Nonneutral Plasma Physics IV*, 10 (2002).
3. M. Amoretti *et al.*, *Nature* 419, 456 (2002).
4. G. B. Andresen *et al.* (ALPHA Collaboration), *Nat. Phys.* 11, 558 (2011).
5. M. Charlton, J. Eades, D. Horváth, R. J. Hughes, and C. Zimmermann, *Physics Report* 241, 65 (1994).
6. M. H. Holzscheiter, M. Charlton, and M. M. Nieto, *Physics Reports* 402, 1 (2004).
7. P. J. Schultz and K. G. Lynn, *Rev. Mod. Phys.* 60, 701 (1988).
8. R. C. Davidson, *Theory of Nonneutral Plasmas*, (Addison-Wesley, Menlo Park, CA, 1989).
9. F. M. Penning, *Physica* 3, 873 (1936).
10. J. H. Malmberg and C. F. Driscoll, *Phys. Rev. Let.* 44, 654 (1980).
11. L. Eggleston, *Phys. Plasmas* 4, 1196 (1997).
12. K. G. Lynn and R. G. Greaves, (private communication, 2001).
13. C. M. Surko and R. G. Greaves, *Radiat. Phys. Chem.* 68, 419 (2003).
14. L. Brillouin, *Physics Review* 67, 260 (1945).
15. D. H. E. Dubin and T. M. O'Neil, *Rev. Mod. Phys.* 71, 87 (1999).
16. A. Khamehchi *et al.*, (unpublished).
17. D.P. Grote *et al.*, WARP manual, (2000).
18. CPO Users Guide, www.electronoptics.com.
19. High Performance Computing Center, Washington State University, Pullman, WA.

20. R. Courant, K. Friedrichs, and H. Lewyt, IBM J. Res. Dev. 11, 215 (1967).
21. C. J. Baker, J. Jennings, A. Verma, J. Xu, M. H. Weber, and K. G. Lynn, Eur. Phys. J. D 66, 109 (2012).
22. K. Gomberoff, J. Wurtele, A. Friedman, D.P. Grote, and J.-L. Vay, J. Comput. Phys. 225, 1736 (2007).
23. R. H. Cohen, A. Friedman, M. Kireeff Covo, S. M. Lund, and A. W. Molvik, Phys. Plasmas 12, 056708 (2005).
24. C. F. Driscoll and J. K. Malmberg, Phys. Rev. Lett. 50, 167 (1983).
25. T. R. Weber, J. R. Danielson, and C. M. Surko, AIP Conf. Proc. 1114, 171 (2009).